The Astrophysical Journal, 972:44 (13pp), 2024 September 1 https://doi.org/10.3847/1538-4357/ad5a04

Revealing the Production Mechanism of High-energy Neutrinos from NGC 1068

Abhishek Das[1,2,3], B. Theodore Zhang[4], and Kohta Murase[1,2,3,4]

[1] Department of Physics, The Pennsylvania State University, University Park, PA 16802, USA
[2] Department of Astronomy & Astrophysics, The Pennsylvania State University, University Park, PA 16802, USA
[3] Center for Multimessenger Astrophysics, Institute for Gravitation and the Cosmos, The Pennsylvania State University, University Park, PA 16802, USA
[4] Center for Gravitational Physics and Quantum Information, Yukawa Institute for Theoretical Physics, Kyoto University, Kyoto 606-8502, Japan

Received 2024 May 17; revised 2024 June 11; accepted 2024 June 18; published 2024 August 23

Abstract

The detection of high-energy neutrino signals from the nearby Seyfert galaxy NGC 1068 provides us with an opportunity to study nonthermal processes near the center of supermassive black holes. Using the IceCube and latest Fermi-LAT data, we present general multimessenger constraints on the energetics of cosmic rays and the size of neutrino emission regions. In the photohadronic scenario, the required cosmic-ray luminosity should be larger than $\sim 1\% - 10\%$ of the Eddington luminosity and the emission radius should be $\lesssim 15 R_{\rm S}$ in low-β plasma and $\lesssim 3 R_{\rm S}$ in high-β plasma. The leptonic scenario overshoots the NuSTAR or Fermi-LAT data for any emission radii we consider, and the required gamma-ray luminosity is much larger than the Eddington luminosity. The beta-decay scenario also violates not only the energetics requirement but also gamma-ray constraints, especially when the Bethe–Heitler and photomeson production processes are consistently considered. Our results rule out the leptonic and beta-decay scenarios in a nearly model-independent manner and support hadronic mechanisms in magnetically powered coronae if NGC 1068 is a source of high-energy neutrinos.

Unified Astronomy Thesaurus concepts: Active galaxies (17); Galaxy jets (601); Neutrino astronomy (1100); Non-thermal radiation sources (1119); Particle astrophysics (96); Gamma-ray astronomy (628); Supermassive black holes (1663)

1. Introduction

The sources of high-energy cosmic neutrinos have remained a big mystery since the discovery by the IceCube Collaboration (Aartsen et al. 2013a, 2013b). Inelastic hadronuclear (pp) and/or photohadronic ($p\gamma$) processes that generate neutrinos should also produce gamma rays of similar energies. The multimessenger observations of the all-sky neutrino and gamma-ray fluxes led to the conclusion that the dominant sources of $10-100$ TeV neutrinos in the range are hidden or opaque for GeV–TeV gamma rays (Murase et al. 2013, 2016; Capanema et al. 2020; Fang et al. 2022). Recently, the IceCube Collaboration reported an excess of 79 events with a global significance of 4.2σ (Abbasi et al. 2022). These neutrinos are observed in the ~ 1.5 to ~ 15 TeV energy range, which leads to a neutrino luminosity about one or two orders of magnitude larger than the gamma-ray luminosity in the GeV–TeV energy range (Acciari et al. 2019; Abdollahi et al. 2020; Ajello et al. 2020, 2023). This implies that the source must be opaque to gamma rays, which supports the results from the diffuse background observations. Therefore, NGC 1068 is treated as a hidden neutrino source, and particle acceleration and secondary emission are very likely in the inner disk and corona regions. The multimessenger data constrain the size of the emission region to $\lesssim 30 R_{\rm S} - 100 R_{\rm S}$, where $R_{\rm S}$ is the Schwarzschild radius (Murase 2022). The population of jet-quiet active galactic nuclei (AGNs) can explain the all-sky neutrino flux, particularly in the 10–100 TeV range (Murase et al. 2020; Eichmann et al. 2022; Padovani et al. 2024), and higher energies may be explained by jet-loud AGNs (Fang & Murase 2018) or low-luminosity AGNs (Kimura et al. 2015, 2021).

The mechanisms of high-energy neutrino emission and particle acceleration in the vicinity of supermassive black holes (SMBHs) have been under debate (for a review see Murase & Stecker 2023, and references therein). It is believed that Seyfert galaxies and quasars commonly have a big blue bump that is attributed to multitemperature blackbody emission from an accretion disk, as well as power-law X-ray emission from a hot plasma region called a corona. Some mechanisms rely on magnetically powered corona models, where particles are accelerated by turbulence and/or magnetic reconnections in low-β plasma (Murase et al. 2020; Kheirandish et al. 2021; Eichmann et al. 2022; Mbarek et al. 2024; Fiorillo et al. 2024). Other mechanisms involve shocks, which could be caused by the freefall of the material (Inoue et al. 2020), failed winds (Inoue et al. 2023), and reconnection-driven flows (Murase 2022), where the plasma is not magnetically dominated. High-energy neutrinos are presumably produced via hadronic processes, but in principle they could also be produced by leptonic processes (e.g., Bhattacharjee & Sigl 2000; Athar et al. 2001; Li & Waxman 2007; Hooper & Plant 2023) and neutron decay from the photodisintegration (e.g., Murase & Beacom 2010b; Zhang et al. 2014; Yasuda et al. 2024).

In this work, we constrain the power of cosmic rays required to explain the observed neutrino fluxes from NGC 1068 considering photohadronic, leptonic, and beta-decay scenarios. We explore the parameter space of the injected cosmic-ray or gamma-ray luminosity required to explain the IceCube data in the relevant energy range and revisit constraints on the emission region together with the latest high-energy gamma-ray data from Fermi-LAT (Ajello et al. 2023).

Our paper is organized as follows. In Section 2, we describe the details of the method used in this work. In Sections 3 and 4, we present the results related to the photohadronic and leptonic scenarios, respectively. In Section 5, we show results related to the beta-decay scenario. We discuss the implications of our results in Section 6. Finally, we give a summary in Section 7. We use $Q_x = Q/10^x$ in CGS units.

2. Method of Calculations

NGC 1068 is an archetypal Seyfert II galaxy that consists of an SMBH with an accretion disk. The luminosity distance is set to $d_L = 10$ Mpc (Tully et al. 2009). This value of d_L has been independently inferred by Courtois et al. (2013) and Tikhonov & Galazutdinova (2021). We use a black hole mass of $M_{\rm BH} = 10^7\,M_\odot$ (Woo & Urry 2002; Panessa et al. 2006), which translates to a Schwarzschild radius $R_{\rm S} \equiv 2GM_{\rm BH}/c^2 \simeq 3.0 \times 10^{12}$ cm, where G is the gravitational constant and c is the speed of light. The Eddington luminosity of NGC 1068 is

$$L_{\rm Edd} \simeq 1.3 \times 10^{45}\ {\rm erg\ s^{-1}} \left(\frac{M_{\rm BH}}{10^7\,M_\odot}\right), \tag{1}$$

and for jet-quiet AGNs the luminosities of cosmic-ray protons, electrons, and nuclei are expected to be lower than this luminosity.

In this work, we consider high-energy neutrinos and gamma rays produced in the single emission region with size R. Based on the previous work, which obtained $R \lesssim 30R_{\rm S}$ (Murase 2022) for the photohadronic scenario, we restrict the range of R from $0.5R_{\rm S}$ to $30R_{\rm S}$ to evaluate the cosmic-ray luminosity, $L_{\rm CR}$, which is required to explain the observed neutrino flux. We consider a similar range of R in the leptonic scenario, because larger radii obviously violate gamma-ray constraints (see below). We also assume that the neutrino emission radius is similar to or larger than the X-ray emission region, which is especially reasonable in the corona model for neutrinos. Such a small neutrino emission radius is compatible with the size of magnetically dominated coronae (e.g., Jiang et al. 2019). In the beta-decay scenario, considering the large-scale jet as a cosmic-ray acceleration site (Yasuda et al. 2024), we assume $R \gtrsim 10^5 R_{\rm S} \simeq 0.1$ pc outside the dust torus.

In the photohadronic scenario neutrinos are produced by the photomeson production, while in the beta-decay scenario neutrinos mainly originate from neutrons produced by the photodisintegration. In both scenarios, the Bethe–Heitler pair production is relevant for electromagnetic emission, especially in the context of AGN coronae (Murase et al. 2020). The target photon fields within the emission region consist of three components (e.g., Murase et al. 2020; Inoue et al. 2023; Murase 2022). The first component is X-ray emission coming from the hot corona. Considering the distance $d_L = 10$ Mpc, the X-ray luminosity at the 2−10 keV range is $L_{\rm X}^{2-10} = 3.38 \times 10^{43}\ {\rm erg\ s^{-1}}$ (Marinucci et al. 2016). The X-ray spectrum is known to be described by a power law with a photon index $\Gamma_{\rm cor} = 2$, which is given by

$$\varepsilon \frac{dn_{\rm cor}}{d\varepsilon} = \tilde{n}_{\rm cor} \left(\frac{\varepsilon}{\varepsilon_{\rm cor}^{\rm cut}}\right)^{1-\Gamma_{\rm cor}} \exp\left(-\frac{\varepsilon}{\varepsilon_{\rm cor}^{\rm cut}}\right), \tag{2}$$

where $\tilde{n}_{\rm cor} = \tilde{L}_{\rm cor}/(4\pi R^2 c \varepsilon_{\rm cor}^{\rm cut})$ and $\tilde{L}_{\rm cor} = 2.2 \times 10^{43}\ {\rm erg\ s^{-1}}$. This component is assumed to start at 31.5 eV and has an exponential cutoff energy $\varepsilon_{\rm cor}^{\rm cut} = 2k_{\rm B}T_e = 128$ keV (Bauer et al. 2015). The resulting total coronal luminosity above 2 keV is $L_{\rm cor}^{\rm tot} = 7.84 \times 10^{43}\ {\rm erg\ s^{-1}}$, and the typical number density of X-ray photons at 2 keV is estimated to be $n_{\rm X} \approx \tilde{L}_{\rm cor}/(4\pi R^2 c \varepsilon_{\rm X})$, where $\varepsilon_{\rm X} = 2$ keV is adopted.

The second component consists of multitemperature blackbody emission from the geometrically thin but optically thick disk (Shakura & Sunyaev 1973). Using a power law with a standard index of $\Gamma_{\rm disk} = 2/3$, starting from $\varepsilon_{\rm dm} = 4.7$ eV and a cutoff energy at $\varepsilon_{\rm disk} = 31.5$ eV, this is parameterized as

$$\varepsilon \frac{dn_{\rm disk}}{d\varepsilon} = \tilde{n}_{\rm disk} \left(\frac{\varepsilon}{\varepsilon_{\rm disk}}\right)^{1-\Gamma_{\rm disk}} \exp\left(-\frac{\varepsilon}{\varepsilon_{\rm disk}}\right), \tag{3}$$

where $\tilde{n}_{\rm disk} = \tilde{L}_{\rm disk}/(4\pi c R^2 \varepsilon_{\rm disk})$ and $\tilde{L}_{\rm disk} = 5.6 \times 10^{44}\ {\rm erg\ s^{-1}}$ (Inoue et al. 2023). Some of the disk emission is reprocessed in the broad-line regions and dust torus, and $L_{\rm bol} = 4.82 \times 10^{44}\ {\rm erg\ s^{-1}}$ represents the bolometric luminosity (Woo & Urry 2002), implying that the Eddington ratio $\lambda_{\rm Edd} \equiv L_{\rm bol}/L_{\rm Edd}$ should be ∼0.4–0.5.

High-energy gamma rays and electrons/positrons, produced from $p\gamma$ interactions, would further interact with the ambient magnetic field and target photon fields, triggering an electromagnetic cascade process. We utilize the ASTROPHYSICAL MULTIMESSENGER EMISSION SIMULATOR (AMES) to simulate photohadronic and photonuclear interactions of high-energy protons and nuclei with target photons within the emission region (see the details of the method in Appendix A of Zhang & Murase 2023), by which we solve coupled time-dependent kinetic equations for photons, electrons/positrons, neutrinos, protons, neutrons, and nuclei (see also the Appendix of Murase 2018). For cosmic-ray protons and nuclei, we consider the photomeson production, photodisintegration, Bethe–Heitler pair production, and synchrotron energy-loss processes. We adopt the continuous energy-loss approximation for synchrotron and inverse Compton processes for electrons/positrons, protons, and nuclei. In the leptonic scenario, AMES also allows us to consider the decay products of muon and antimuon pairs, including both neutrinos and electrons/positrons, which are produced from the two-photon annihilation process.

In this work, the magnetic field energy density is parameterized by the bolometric luminosity, as $U_B = \xi_B U_\gamma$, where $U_B = B^2/8\pi$ is the magnetic energy density and $U_\gamma = L_{\rm bol}/(4\pi R^2 c)$ is the bolometric photon energy density. Given that the equipartition parameter is $\xi_B \lesssim 1$ for a near-Eddington system such as NGC 1068, we calculate spectra for $\xi_B = 1$, 0.1, and 0.01. We assume no escape for charged particles, while the escape time of neutral particles is set to $t_{\rm esc} = R/c$. We solve the kinetic equations during the dynamical time, $t_{\rm dyn} = R/V$. Although $V = 0.1c$ is adopted as a default value, we will see that our conclusions are unaffected by this choice.

Finally, as in Murase (2022), we take into account gamma-ray attenuation due to matter interactions due to the Bethe–Heitler pair production (Chodorowski et al. 1992) and Compton scatterings, where we use a column density of $N_{\rm H} = 10^{25}\ {\rm cm^{-2}}$ (Marinucci et al. 2016). High-energy gamma rays above TeV energies can further be attenuated by infrared emission from the dust torus, whose innermost region has a fiducial radius of $R_{\rm DT} = 0.1$ pc (Imanishi et al. 2016; García-Burillo et al. 2019). The spectrum is approximated by a blackbody with a temperature of $T_{\rm DT} = 1000$ K (Inoue et al.

2023; Rosas et al. 2022) as

$$\varepsilon \frac{dn_{\rm DT}}{d\varepsilon} = \frac{8\pi}{c^3 h^3} \frac{\varepsilon^3}{\exp(\varepsilon / k_{\rm B} T_{\rm DT}) - 1}. \tag{4}$$

We multiply cascaded photon spectra by an attenuation factor, $\exp(-\tau_{\gamma\gamma}^{\rm DT})$, where $\tau_{\gamma\gamma}^{\rm DT} = t_{\gamma\gamma}^{-1} R_{\rm DT}/c$ and $t_{\gamma\gamma}$ is the $\gamma\gamma$ interaction timescale in the infrared photon field. Note that the energies of the photons making up this component are well below the threshold for neutrino production, and our results on neutrinos are unaffected by the implementation of this component.

2.1. Optical Depths

The effective optical depth to the Bethe–Heitler pair production process in the disk photon field is estimated to be (e.g., Murase et al. 2020)

$$\begin{aligned} f_{\rm BH} &\approx \tilde{n}_{\rm disk} \hat{\sigma}_{\rm BH} R (c/V) \\ &\simeq 7.0 \tilde{L}_{\rm disk,\,44.7} \left(\frac{R}{10 R_{\rm S}}\right)^{-1} \left(\frac{M_{\rm BH}}{10^7\, M_\odot}\right)^{-1} \\ &\times \left(\frac{\varepsilon_{\rm disk}}{31.5\ {\rm eV}}\right)^{-1} \left(\frac{V}{0.1 c}\right)^{-1}, \end{aligned} \tag{5}$$

where $\hat{\sigma}_{\rm BH} \sim 0.8 \times 10^{-30}\ {\rm cm}^2$ and the typical proton energy causing pair production is $\tilde{\varepsilon}_p^{\rm BH-disk} \approx 0.5 \bar{\varepsilon}_{\rm BH} m_p c^2 / \varepsilon_{\rm disk} \simeq 1.5 \times 10^5\ {\rm GeV}\ (\varepsilon_{\rm disk}/31.5\ {\rm eV})^{-1}$ and $\bar{\varepsilon}_{\rm BH} \approx 10$ MeV. In the photohadronic scenario, TeV neutrinos mostly come from interactions with X-ray photons, and the effective optical depth to the photomeson production process is estimated to be

$$\begin{aligned} f_{p\gamma} &\approx \eta_{p\gamma} \hat{\sigma}_{p\gamma} R (c/V) \tilde{n}_{\rm X} \left(\frac{\varepsilon_p}{\tilde{\varepsilon}_p^{p\gamma-X}}\right)^{\Gamma_{\rm cor}-1} \\ &\simeq 0.39\, \eta_{p\gamma} \tilde{L}_{\rm cor,43.3} \left(\frac{R}{10 R_S}\right)^{-1} \left(\frac{M_{\rm BH}}{10^7 M_\odot}\right)^{-1} \\ &\times \left(\frac{V}{0.1 c}\right)^{-1} \left(\frac{\varepsilon_p}{\tilde{\varepsilon}_p^{p\gamma-X}}\right)^{\Gamma_{\rm cor}-1}, \end{aligned} \tag{6}$$

where $\eta_{p\gamma} = 2/(1 + \Gamma_{\rm cor})$, $\hat{\sigma}_{p\gamma} \sim 0.7 \times 10^{-28}\ {\rm cm}^2$, and $\tilde{\varepsilon}_p^{p\gamma-{\rm X}} \simeq 7.9 \times 10^4\ {\rm GeV}\ (\varepsilon_{\rm X}/2{\rm keV})^{-1}$. We can see that, at ∼10 TeV, proton energy losses via the Bethe–Heitler pair production process are more significant than the photomeson production (as shown in Murase 2022), which is consistent with Figure 1.

The optical depths to electron–positron and muon–antimuon pair production from the two-photon annihilation process are shown in Figure 1. For the electron–positron pair production, the threshold gamma-ray energy is $\tilde{\varepsilon}_\gamma^{e^+e^--{\rm X}} \approx m_e^2 c^4 / \varepsilon_{\rm X} \simeq 0.13\ {\rm GeV}\ (\varepsilon_{\rm X}/2{\rm keV})^{-1}$, and the two-photon annihilation optical depth to electron–positron pair production in the GeV gamma-ray range is (Murase 2022)

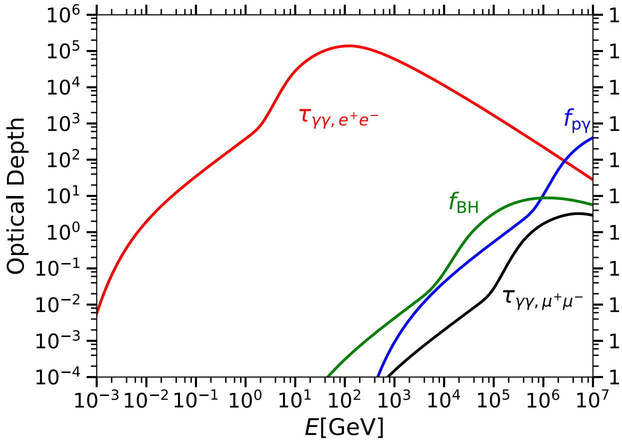

Figure 1. Optical depths for two-photon annihilation, either electron–positron pair production or muon–antimuon pair production, and effective optical depths for photomeson production and Bethe–Heitler pair production. The emission radius is set to $R = 10 R_{\rm S}$. For the photomeson production and the Bethe–Heitler process, the proton escape timescale is set to $t_* = 10 R/c$.

$$\begin{aligned} \tau_{\gamma\gamma\to e^+e^-} &\approx \eta_{\gamma\gamma} \sigma_{\rm T} R \tilde{n}_{\rm X} \left(\frac{\varepsilon_\gamma}{\tilde{\varepsilon}_\gamma^{e^+e^--{\rm X}}}\right)^{\Gamma_{\rm cor}-1} \\ &\simeq 44\, \tilde{L}_{\rm cor,43.3} \left(\frac{R}{10 R_{\rm S}}\right)^{-1} \left(\frac{M_{\rm BH}}{10^7 M_\odot}\right)^{-1} \\ &\times \left(\frac{\varepsilon_\gamma}{\tilde{\varepsilon}_\gamma^{e^+e^--{\rm X}}}\right)^{\Gamma_{\rm cor}-1}, \end{aligned} \tag{7}$$

where $\eta_{\gamma\gamma} \approx 0.12$ is the coefficient (Svensson 1987) and $\sigma_{\rm T} \approx 6.65 \times 10^{-25}\ {\rm cm}^2$ is the Thomson cross section. The two-photon annihilation optical depth to muon–antimuon pair production is

$$\begin{aligned} \tau_{\gamma\gamma\to\mu^+\mu^-} &\approx \eta_{\gamma\gamma} (m_e/m_\mu)^2 \sigma_{\rm T} R \tilde{n}_{\rm X} \left(\frac{\varepsilon_\gamma}{\tilde{\varepsilon}_\gamma^{\mu^+\mu^--X}}\right)^{\Gamma_{\rm cor}-1} \\ &\simeq 1.0 \times 10^{-3}\, \tilde{L}_{\rm cor,\,43.3} \left(\frac{R}{10 R_{\rm S}}\right)^{-1} \left(\frac{M_{\rm BH}}{10^7\, M_\odot}\right)^{-1} \\ &\times \left(\frac{\varepsilon_\gamma}{\tilde{\varepsilon}_\gamma^{\mu^+\mu^--X}}\right)^{\Gamma_{\rm cor}-1}, \end{aligned} \tag{8}$$

where $\tilde{\varepsilon}_\gamma^{\mu^+\mu^--{\rm X}} \approx m_\mu^2 c^4 / \varepsilon_{\rm X} \simeq 5.6 \times 10^3\ {\rm GeV}\ (\varepsilon_{\rm X}/2{\rm keV})^{-1}$. The above expressions for $\tau_{\gamma\gamma\to e^+e^-}$ and $\tau_{\gamma\gamma\to\mu^+\mu^-}$ are consistent with the numerical results shown in Figure 1. We can also see that the optical depth to the electron–positron pair production at ∼10 TeV is $\sim 10^6$ larger than that to the muon–antimuon pair production.

3. Photohadronic Scenario

We assume that the injected cosmic-ray proton spectrum follows a power-law distribution with an exponential cutoff,

$$\frac{d\dot{n}_{\rm CR}}{d\varepsilon_p} \propto \varepsilon_p^{-s_{\rm CR}} \exp\left(-\frac{\varepsilon_p}{\varepsilon_p^{\max}}\right), \tag{9}$$

where $s_{\rm CR}$ is the proton power-law index and $\varepsilon_p^{\rm max}$ is the proton maximum energy. The normalization is set by the cosmic-ray proton luminosity, which is

$$L_{\rm CR} = \mathcal{V}\int_{\varepsilon_p^{\rm min}}^{\infty} \varepsilon_p \frac{d\dot{n}_{\rm CR}}{d\varepsilon_p} d\varepsilon_p, \tag{10}$$

where $\mathcal{V} = (4\pi/3)R^3$ is the volume of the emission region. We perform simulations for $\varepsilon_p^{\rm min} = 10$ TeV and $\varepsilon_p^{\rm max} = 30$ TeV but vary the spectral index, $s_{\rm CR}$, from 1 to 4. Below $\varepsilon_p^{\rm min} = 10$ TeV, a sufficiently hard spectrum is required not to violate the energetics requirement (Murase 2022). Since the observed neutrino flux is extended down to $\varepsilon_\nu \sim 1$ TeV, corresponding to a parent proton energy of $\varepsilon_p \sim 20\varepsilon_\nu \sim 20$ TeV, it is reasonable to adopt a low-energy cutoff at $\varepsilon_p^{\rm min} = 10$ TeV to evaluate the minimum cosmic-ray proton luminosity. The value of $\varepsilon_p^{\rm max} = 30$ TeV is a conservative choice as the high-energy cutoff for the purpose of evaluating $L_{\rm CR}$. A larger value results in more neutrinos with higher energies, which in turn requires a larger value of $L_{\rm CR}$, while the 1.5–15 TeV neutrino flux may match the IceCube data.

The injected cosmic-ray luminosity, $L_{\rm CR}$, is constrained by comparing the all-flavor neutrino luminosity between 1.5 and 15 TeV to the value obtained by the IceCube Collaboration, $L_\nu = (1.4 \pm 0.53) \times 10^{42}$ erg s^{-1} (Abbasi et al. 2022). Note that we set the luminosity distance to $d_L = 10$ Mpc, which is shorter than the luminosity distance $d_L = 14.4$ Mpc used in Abbasi et al. (2022).

3.1. Multimessenger Spectra and Gamma-Ray Constraints

We show cascaded photon and all-flavor neutrino spectra in Figure 2 for different emission radii with $R = 0.5R_{\rm S}$, $3R_{\rm S}$, $10R_{\rm S}$, and $30R_{\rm S}$, respectively. The neutrino spectra are shown with dashed lines, while the cascade photon spectra are shown with solid lines. We also depict the intrinsic flux of X-rays with dotted lines. Note that the cascade flux in the X-ray range is lower than the intrinsic X-ray flux from coronae, as shown in previous works (Murase et al. 2020; Murase 2022), so that constraints from X-ray observations are much weaker than those from gamma-ray observations. The AGN corona model itself predicts that the neutrino luminosity is approximately proportional to the X-ray luminosity (Murase & Waxman 2016; Murase et al. 2020), and the cosmic-ray luminosity is expected to be lower than the X-ray luminosity (Murase et al. 2016).

The cascaded photon spectra vary with emission radii. For larger emission radii, e.g., $R = 30R_{\rm S}$, the cascade photon spectra overshoot the Fermi-LAT data obtained from sub-GeV to GeV energies (Ajello et al. 2023), especially for $\xi_B = 0.1$ and $\xi_B = 0.01$. While our numerical results confirm those of Murase (2022), the gamma-ray data adopted in this work (Ajello et al. 2023) extend to lower and higher energies, which give tighter constraints on R. The synchrotron cascade with $\xi_B \gtrsim 0.1$ allows more parameter space for R, because more gamma rays appear at sub-GeV or lower energies.

Then, we obtain gamma-ray constraints on emission radii by requiring the cascade photon spectra from our simulations not to overshoot the measured gamma-ray data, especially the lowest-energy Fermi-LAT upper limit at the 95% confidence level. Our results are represented by the red and orange curves in Figure 3, which are calculated for $\xi_B = 1.0$ and $\xi_B = 0.01$, respectively. We find that the size of the emission region is constrained to $R \lesssim 15R_{\rm S}$ for $\xi_B = 1.0$ and to $R \lesssim 3R_{\rm S}$ for $\xi_B = 0.01$. The constraints are tighter for softer spectral indices of the injected proton spectrum. This is because a softer cosmic-ray spectrum results in more Bethe–Heitler pair production processes that give rise to larger cascaded photon fluxes.

Our constraints on R for $\xi_B \lesssim 0.01$ imply that the neutrino emission region is unlikely to be high-β plasma if NGC 1068 is a Schwarzschild black hole. This is because the upper limits on R are smaller than the innermost stable circular orbit (ISCO) for the nonrotating case. While it does not exclude ISCOs for a Kerr black hole with prograde orbits, given that NGC 1068 does not have a strong jet, an extreme Kerr black hole might also be disfavored, although details depend on the magnetic flux configuration.

3.2. Required Power from Neutrino Observations

In Figure 3, we show the required cosmic-ray proton luminosity as a function of R and $s_{\rm CR}$. We find that the typical range of the injected cosmic-ray luminosity for our chosen parameter space is $L_{\rm CR} \sim (3-30) \times 10^{43}$ erg s^{-1}, which is less than the bolometric and Eddington luminosities of NGC 1068. From Equation (6), we see that the efficiency for neutrino production is proportional to R^{-1}, which means that smaller radii are preferred for efficient neutrino production. Correspondingly, the required minimum cosmic-ray luminosity may decrease with emission radii.

On the other hand, harder spectral indices could alleviate the required cosmic-ray power. While the IceCube data provide the best-fit spectrum with a spectral index of 3.2 (Abbasi et al. 2022), hard spectra with a cutoff may explain the data (Murase 2022). For $s_{\rm CR} \lesssim 2$, protons with energy around $\varepsilon_p^{\rm max}$ are dominant. Therefore, the $L_{\rm CR}$ requirement changes drastically upon going from $s_{\rm CR} = 1$ to $s_{\rm CR} = 2$, as it mostly increases the density of lower-energy protons that do not contribute to neutrino production. For $s_{\rm CR} \lesssim 2$, protons with energy around $\varepsilon_p^{\rm min}$ are dominant. Therefore, further increasing the softness does not affect the required $L_{\rm CR}$ much.

The minimum cosmic-ray proton power is estimated to be

$$L_{\rm CR} \gtrsim (3-30) \times 10^{43}\ {\rm erg\ s^{-1}}, \tag{11}$$

which can be below the bolometric and Eddington luminosities, so we conclude that the photohadronic scenario is viable as a mechanism for neutrino emission from NGC 1068.

4. Leptonic Scenario

In principle, neutrinos could be produced by a pure leptonic process through the two-photon annihilation and muon–antimuon pair production (e.g., Li & Waxman 2007, as an example for neutrino production in intergalactic space). This process can be relevant only at sufficiently high energies, where electron–positron pair production is highly suppressed by Klein–Nishina-like effects. The decay of muons and antimuons will then produce neutrinos without involving the acceleration of cosmic-ray protons and nuclei. Assuming that very high-energy gamma rays are produced, Hooper & Plant (2023) argued that primary electrons with a luminosity of $L_e \sim 10^{42}$–10^{43} erg s^{-1} injected above 1 TeV are needed to explain the observed neutrino flux. In addition, considering kilogauss-scale magnetic fields and dense keV-scale target

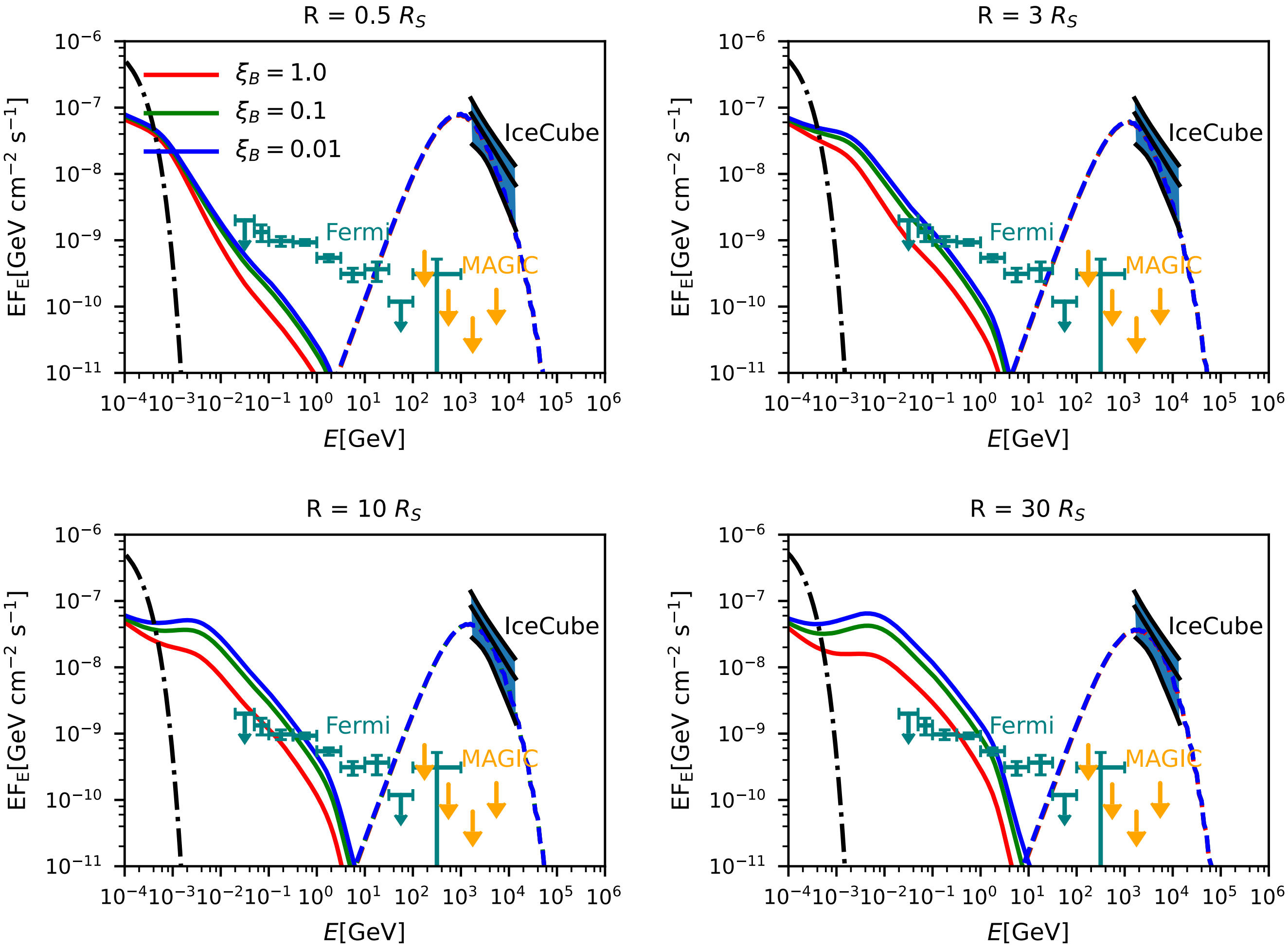

Figure 2. Cascaded photon spectra (solid curves) and all-flavor neutrino spectra (dashed lines curves) for different values of R and ξ_B in the photohadronic scenario. All plots are made using parameters for injected cosmic-ray protons, $s_{\rm CR} = 2$, $\varepsilon_p^{\rm min} = 10$ TeV, and $\varepsilon_p^{\rm max} = 30$ TeV. The black lines correspond to the 95% contour lines and line of best fit from the IceCube data (Abbasi et al. 2022). Gamma-ray data from the Fermi-LAT (Ajello et al. 2023) and MAGIC (Acciari et al. 2019) observations are also shown. The tail of the intrinsic X-ray flux used in the calculation is represented by the dashed–dotted curves.

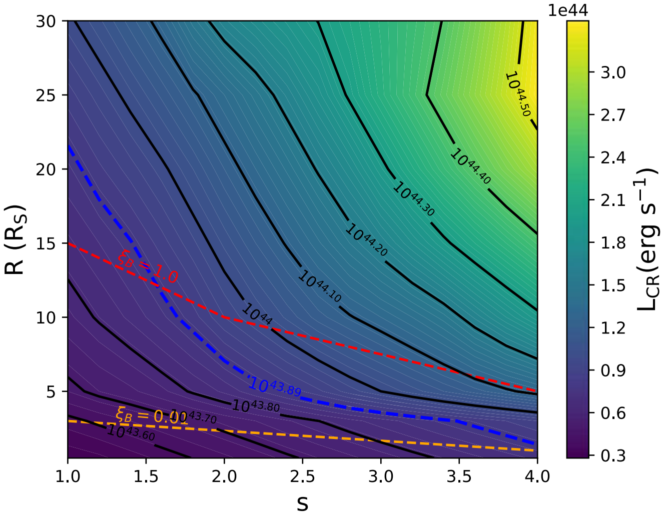

Figure 3. Required minimum cosmic-ray proton luminosity, $L_{\rm CR}$, as a function of the emission radius R and power-law index $s_{\rm CR}$ for $\varepsilon_p^{\rm min} = 10$ TeV, $\varepsilon_p^{\rm max} = 30$ TeV, and $\xi_B = 1.0$ in the photohadronic scenario. Regions above the red and orange dashed lines are excluded by the Fermi-LAT data (Ajello et al. 2023) for $\xi_B = 1.0$ and $\xi_B = 0.01$, respectively. The blue contour corresponds to $L_{\rm cor}^{\rm tot}$, which is the total coronal luminosity.

photons, they adopted a blackbody spectrum with a temperature of $T = 1$–10 keV as a target photon field.

In this work, we consider the realistic target photon fields discussed in Section 2 to test this scenario. We will show that the multiwavelength data observed at the low-energy gamma-ray band (Acciari et al. 2019; Ajello et al. 2023) give strong constraints on this scenario, considering that the associated electromagnetic cascade process is unavoidable. For the purpose of this work, we inject a power-law spectrum of high-energy gamma rays with an exponential cutoff at both low- and high-energy parts, which is written as

$$\frac{d\dot{n}_\gamma}{d\varepsilon_\gamma} \propto \varepsilon_\gamma^{-s_\gamma} \exp\left(-\frac{\varepsilon_\gamma^{\rm min}}{\varepsilon_\gamma}\right) \exp\left(-\frac{\varepsilon_\gamma}{\varepsilon_\gamma^{\rm max}}\right), \tag{12}$$

where $\varepsilon_\gamma^{\rm min} = 12$ TeV and $\varepsilon_\gamma^{\rm max} = 15$ TeV. As in the photohadronic scenario, we consider a range of spectral index of the injected gamma-ray spectrum, s_γ, between 1 and 4. The total injected gamma-ray luminosity is given by

$$L_\gamma = \mathcal{V} \int_{-\infty}^{\infty} d\varepsilon_\gamma \frac{d\dot{n}_\gamma}{d\varepsilon_\gamma} \varepsilon_\gamma. \tag{13}$$

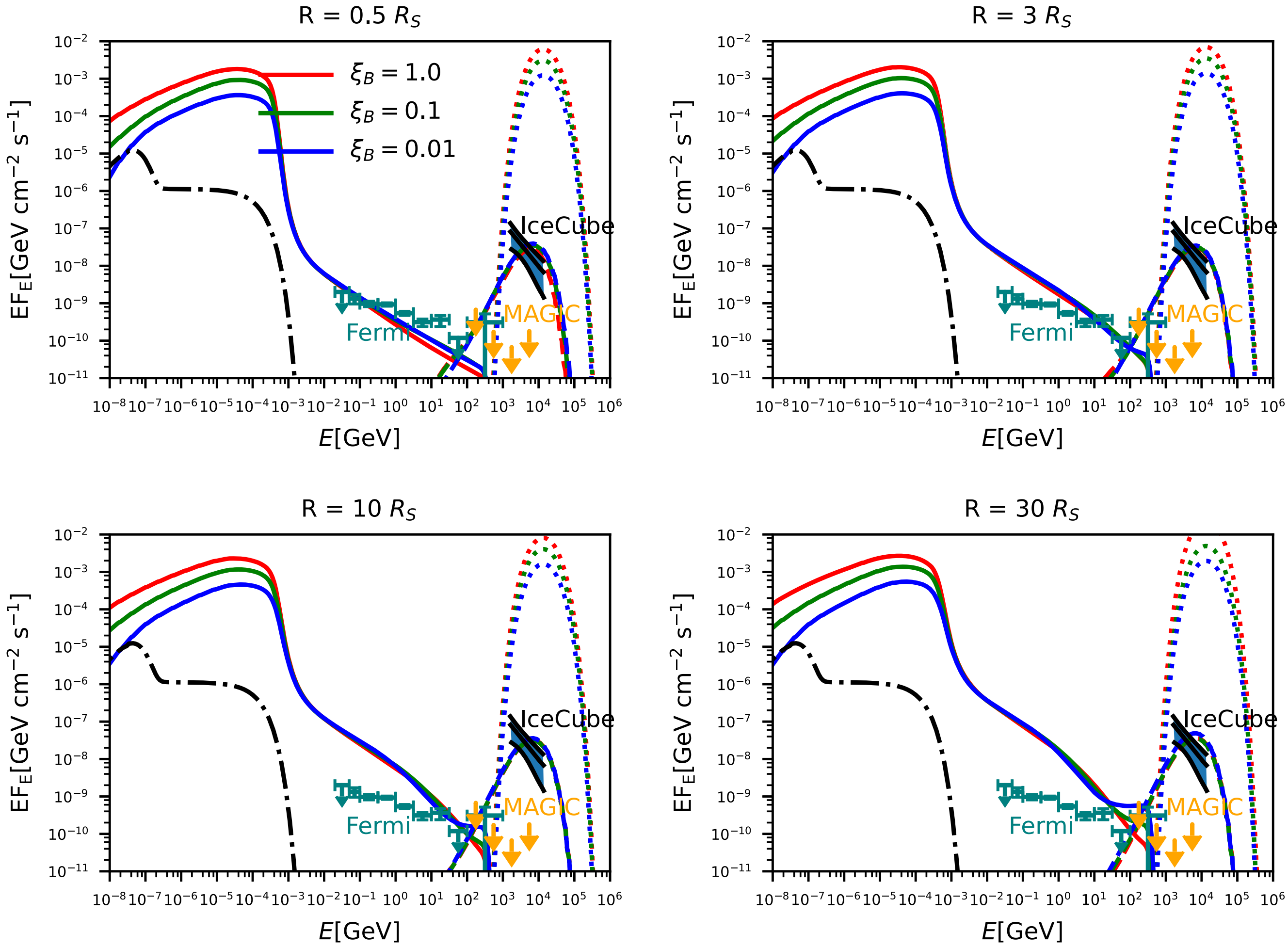

Figure 4. Same as in Figure 2, but we show cascaded photon spectra and all-flavor neutrino spectra (solid and dashed lines, respectively) for different values of R and ξ_B in the leptonic scenario. All panels are made using parameter values $s_\gamma = 2.0$, $\varepsilon_\gamma^{\rm min} = 12$ TeV, and $\varepsilon_\gamma^{\rm max} = 15$ TeV for the injected photon spectrum.

4.1. Multimessenger Spectra and Gamma-Ray Constraints

In Figure 4, we show cascaded photon and all-flavor neutrino spectra in the leptonic scenario (solid and dashed lines, respectively). The injected gamma-ray spectra are shown using dotted lines. The injected gamma rays interact with the disk and coronal photons, and some of them produce muon–antimuon pairs. Most of the gamma rays are cascaded down to MeV or lower energies and overwhelm the intrinsic coronal spectrum.

We also examine cascade constraints as in the photohadronc scenario. In the leptonic scenario, we find that the cascaded photon spectra violate gamma-ray observations including the Fermi-LAT data (Ajello et al. 2023) for almost the entire region of parameter space that we test. In addition, the cascaded X-ray flux is much larger than the intrinsic X-ray flux inferred by NuSTAR observations (represented by the dotted–dashed line). We do not find a viable parameter space for the leptonic scenario to explain the observed IceCube data (Abbasi et al. 2022) without violating the intrinsic X-ray or gamma-ray data.

This situation can be understood as follows. At $\varepsilon_\gamma \gtrsim$ a few GeV, the two-photon annihilation optical depth for electron–positron pair production is expected to be dominated by the interaction with disk photons or other optical and ultraviolet photons if they exist. The optical depth at $\gtrsim$10–100 GeV is naively estimated by the following expression:

$$\tau_{\gamma\gamma\to e^+e^-} \simeq 1.1\times10^6\left(\frac{\tilde{\varepsilon}_\gamma^{e^+e^- - \rm dm}}{\tilde{\varepsilon}_\gamma^{e^+e^- - \rm disk}}\right)^{-1/3}\left(\frac{\varepsilon_\gamma}{\tilde{\varepsilon}_\gamma^{e^+e^- - \rm dm}}\right)^{-1} \times \tilde{L}_{\rm disk,\,44.7}\left(\frac{R}{10R_{\rm S}}\right)^{-1}\left(\frac{M_{\rm BH}}{10^7\,M_\odot}\right)^{-1}\Lambda_1, \quad (14)$$

where $\tilde{\varepsilon}_\gamma^{e^+e^- - \rm disk} \approx m_e^2c^4/\varepsilon_{\rm disk} \simeq 8.3$ GeV $(\varepsilon_{\rm disk}/31.5\ {\rm eV})^{-1}$, $\tilde{\varepsilon}_\gamma^{e^+e^- - \rm dm} \approx m_e^2c^4/\varepsilon_{\rm dm} \simeq 56$ GeV $(\varepsilon_{\rm dm}/4.7\ {\rm eV})^{-1}$, and Λ is the logarithmic factor. In the leptonic scenario, neutrinos in the TeV range are mostly produced via interactions with coronal photons or other high-energy photons originating from electromagnetic cascades.

For given $\varepsilon_{\rm X}$ and $\varepsilon_{\rm disk}$, with $\Gamma_{\rm cor} = 2$, the ratio of the above two optical depths at sufficiently high energies is estimated by

$$\frac{\tau_{\gamma\gamma\to e^+e^-}}{\tau_{\gamma\gamma\to\mu^+\mu^-}} \sim 2\times10^6\left(\frac{\tilde{L}_{\rm disk,\,44.7}}{\tilde{L}_{\rm cor,\,43.3}}\right)\Lambda_1, \quad (15)$$

which roughly agrees with the numerical result shown in Figure 1. This ratio is also consistent with that of the gamma-ray flux to the neutrino flux shown in Figure 4. For comparison, Hooper & Plant (2023) argued that the ratio is ∼0.1–0.01 for the optical depth at around 10 TeV assuming a blackbody

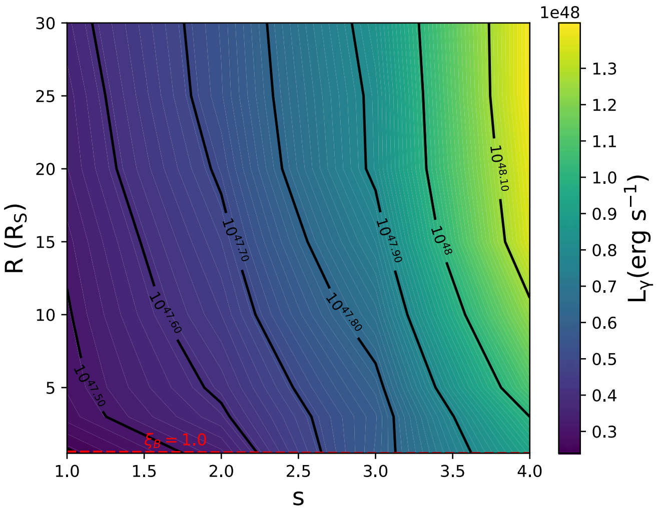

Figure 5. Required minimum gamma-ray luminosity, L_γ, as a function of R and s_γ, for $\varepsilon_\gamma^{\min} = 12$ TeV, $\varepsilon_\gamma^{\max} = 15$ TeV, and $\xi_B = 1.0$, in the leptonic scenario. We find that $L_{\rm CR}$ exceeds $L_{\rm bol} \sim L_{\rm Edd}$ in the entire parameter space. The region above the red dashed line is excluded by the Fermi-LAT data (Ajello et al. 2023) for $\xi_B = 1.0$. All parameter space is excluded for $\xi_B = 0.01$.

spectrum with a temperature of 1 keV. For a realistic X-ray spectrum that is described by a power law, as shown in this work, the ratio is much larger, which is the reason why the contribution of neutrinos from muon–antimuon production was not usually shown in the previous calculations (Murase 2022).

4.2. Required Power from Neutrino Observations

As seen in Figure 5, we calculate the required power of injected gamma rays, which is $L_\gamma \sim (1{-}4) \times 10^{47}$ erg s^{-1}, to explain the observed neutrino flux in the leptonic scenario. These values are about two orders of magnitude greater than the bolometric luminosity. Our results on the required power of injected gamma rays are also about four orders larger than the required electron luminosity derived in Hooper & Plant (2023). The difference is that we adopt a realistic coronal photon field with a differential energy density of $\tilde{U}_{\rm cor} \simeq 5.9 \times 10^4$ erg cm^{-3} $(R/10R_{\rm S})^{-2}\tilde{L}_{\rm cor,43.3}$, which is many orders smaller than the energy density of the blackbody photon field with a temperature of $k_{\rm B}T = 1$ keV.

Compared to the required cosmic-ray power in the photohadronic scenario, the required power of injected gamma rays in the leptonic scenario is insensitive to the size of the emission region, as shown in Figure 3. The reason is that, for environments that are optically thick to electron–positron pair production, the neutrino flux is determined by the ratio between muon–antimuon and electron–positron pair production. Analytically, considering $\tau_{\gamma\gamma\to e^+e^-} \gg 1$, the all-flavor neutrino flux is estimated by

$$\varepsilon_\nu \frac{dL_{\varepsilon_\nu}}{d\varepsilon_\nu} \approx \frac{2}{3}\frac{\tau_{\gamma\gamma\to\mu^+\mu^-}}{\tau_{\gamma\gamma\to e^+e^-}}\varepsilon_\gamma \frac{dL_{\varepsilon_\gamma}}{d\varepsilon_\gamma}. \tag{16}$$

Given that the ratio is $\sim 10^5{-}10^6$, the minimum gamma-ray power is

$$L_\gamma \sim (10^5 - 10^6)L_\nu \sim (10^{47} - 10^{48}) \text{ erg s}^{-1} \gg L_{\rm bol}. \tag{17}$$

The required minimum gamma-ray luminosity is much larger than the Eddington luminosity, so that we conclude that the muon–antimuon pair production process is excluded as a mechanism for high-energy neutrinos from NGC 1068.

5. Beta-decay Scenario

We assume that the injected cosmic-ray nuclei spectrum follows a power-law distribution with an exponential cutoff,

$$\frac{d\dot{n}_{\rm CR}}{d\varepsilon_A} \propto \varepsilon_A^{-s_{\rm CR}} \exp\left(-\frac{\varepsilon_A}{\varepsilon_A^{\max}}\right), \tag{18}$$

where $s_{\rm CR}$ is the power-law index and $\varepsilon_A^{\max}$ is the maximum energy of cosmic-ray nuclei. For the composition, we assume helium nuclei, but the results are similar for heavier nuclei. The normalization is set by the cosmic-ray luminosity, which is

$$L_{\rm CR} = \mathcal{V}\int_{\varepsilon_A^{\min}}^{\infty} \varepsilon_A \frac{d\dot{n}_{\rm CR}}{d\varepsilon_A} d\varepsilon_A. \tag{19}$$

We adopt the same target photon fields as in the photohadronic and leptonic scenarios. In the beta-decay scenario, as in Yasuda et al. (2024), we assume that the emission region is located outside the dust torus, which is justified if nuclei are accelerated in jets (Pe'er et al. 2009). We consider not only infrared photons from the dust torus but also the cosmic microwave background (CMB) and extragalactic background light (EBL). For target photons from the dust torus, the energy density is assumed to decrease as $(R_{\rm DT}/R)^2$ at $R > R_{\rm DT}$. The mean lifetime of free neutrons is $\tau_n \approx 879.6$ s (Workman et al. 2022), and we consider beta-decay neutrinos from both inside and outside the emission region. The magnetic field strength in the emission region is assumed to be $B = 1\ \mu$G as a default value, but we checked that our conclusions are largely insensitive to this choice because the energy density of the dust component is dominant. For the EBL, we use the model of Gilmore et al. (2012) and take into account gamma-ray attenuation due to CMB and EBL during intergalactic propagation.

5.1. Multimessenger Spectra and Gamma-Ray Constraints

In Figure 6, we show cascaded photon and all-flavor neutrino spectra in the beta-decay scenario (solid and dashed lines, respectively). The injected cosmic-ray spectra are shown with dotted lines. The blue lines consider the photodisintegration process, the photomeson production process, the Bethe–Heitler pair production process, and neutron decay. For comparison purposes, we also show the case without considering the photomeson production process with red lines.

The effective photodisintegration cross section for $A \leqslant 4$ (including inelasticity with $1/A$) is given by $\hat{\sigma}_{\rm dis} \approx 4.3 \times 10^{-28}$ cm^2 $(A/4)^{-2.433}$ (Karakula et al. 1994; Murase & Beacom 2010a). Then, the effective optical depth to photodisintegration for helium nuclei is

$$\begin{aligned} f_{\rm dis} &\approx \tilde{n}_{\rm disk}\hat{\sigma}_{\rm dis}R(c/V) \\ &\simeq 3.8 \times 10^{-4}\, \tilde{L}_{\rm disk,\,44.7}\left(\frac{R}{10^8 R_{\rm S}}\right)^{-1}\left(\frac{M_{\rm BH}}{10^7\,M_\odot}\right)^{-1} \\ &\times\left(\frac{\varepsilon_{\rm disk}}{31.5 \text{ eV}}\right)^{-1}\left(\frac{V}{0.1c}\right)^{-1}, \end{aligned} \tag{20}$$

which can be almost unity at sufficiently small emission radii. Note that a fraction of energy carried by nucleons is only $1/A$

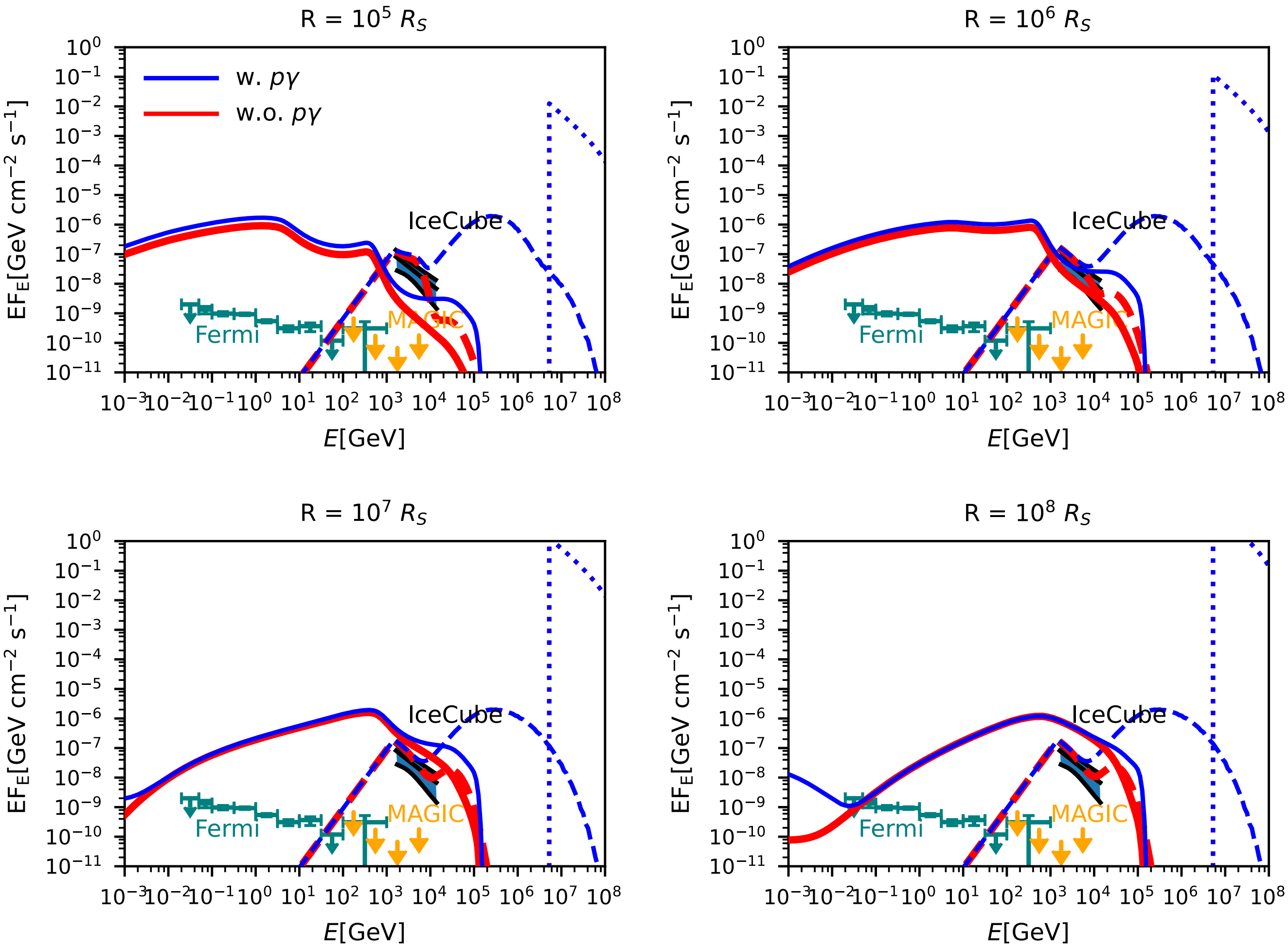

Figure 6. Same as in Figure 2, but we show the cascaded gamma-ray spectra and all-flavor neutrino spectra (solid and dashed lines respectively) for different values of R in the decay scenario. The EBL attenuation is considered (Gilmore et al. 2012). All panels are made using parameter values $s_{\rm CR} = 3.2$, $\varepsilon_A^{\rm min} = 5$ PeV, and $\varepsilon_A^{\rm max} = 100$ PeV for the injected helium nuclei spectrum.

per collision, which should be considered for the calculations of neutrinos and gamma rays (e.g., Murase & Beacom 2010b; Zhang & Murase 2023). In addition, the average energy of neutrinos from neutron decay is 0.48 MeV in the neutron rest frame (e.g., Murase & Beacom 2010b), so the energy fraction carried by neutrinos is $0.48\,{\rm MeV}/(m_n c^2) \sim 1/(2000)$. The average kinetic energy of beta-decay electrons is 0.3 MeV (Zhang & Murase 2023).

One important point is that the Bethe–Heitler pair production process is unavoidable. This is because the threshold for electron–positron production, $2m_ec^2$, is lower than that for nuclear disintegration. A similar efficiency issue exists for de-excitation gamma rays, although the energy range of de-excitation gamma rays is different from that of cascade gamma rays from the Bethe–Heitler pairs and beta-decay electrons (Aharonian & Taylor 2010; Murase & Beacom 2010a; Zhang & Murase 2023). When disk photons are main targets, the ratio of the Bethe–Heitler contribution to the beta-decay contribution is given by

$$\frac{6000 f_{\rm BH}(Z^2/A)}{f_{\rm dis}} \sim 10, \tag{21}$$

where $Z^2/A = 1$ for helium and $f_{\rm BH}$ in Equation (5) is defined for protons. While we find that the cascaded photon spectrum only from beta-decay electrons overshoots the gamma-ray data including the Fermi-LAT data and MAGIC upper limits, this conclusion is robust in the presence of electron–positron pairs from the Bethe–Heitler process.

Note that the electromagnetic cascade is likely to be dominated by inverse Compton emission. The dust field is dominant over CMB and EBL for sufficiently small emission radii that assure efficient photodisintegration, at which the magnetic field is weaker than the equipartition magnetic field,

$$B_{\rm eq} = \sqrt{\frac{8\pi L_{\rm DT}}{4\pi R^2 c}}$$
$$\simeq 0.24\ {\rm G}\ (R/R_{\rm DT})^{-1}(0.1\ {\rm pc}/R_{\rm DT})L_{\rm DT,43.9}^{1/2}. \tag{22}$$

We have also checked the results with a higher value of the magnetic field strength with $B = 300\ \mu$G, and our conclusions remain unchanged. Even though the results remain similar, the cascade photon flux may also be enhanced because of the contribution from synchrotron emission.

Furthermore, the primary gamma-ray component from π^0 decay must exist once the photomeson production is consistently included. The threshold energy for the pion production is higher, but due to the higher efficiency (see also Murase & Beacom 2010b, 2010a), we find that the contribution from the

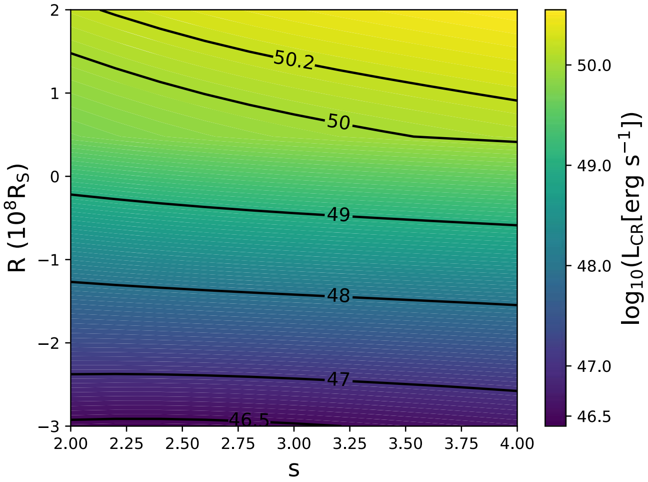

Figure 7. Required minimum cosmic-ray helium luminosity, $L_{\rm CR}$, as a function of R and $s_{\rm CR}$. We find that $L_{\rm CR}$ exceeds $L_{\rm bol} \sim L_{\rm Edd}$ in all the parameter space.

photomeson production is not negligible and violates the MAGIC upper limits independent of magnetic fields.

5.2. Required Power from Neutrino Observations

The minimum cosmic-ray luminosity required from the IceCube neutrino data is shown in Figure 7. We find that the cosmic-ray helium luminosity is $L_{\rm CR} \gtrsim 3 \times 10^{46}$ erg s^{-1} for the whole parameter region. The required cosmic-ray luminosity almost linearly increases with the emission radius, while being less sensitive to the spectral index.

Analytically, the differential muon neutrino luminosity after neutrino mixing is written as

$$\begin{aligned} \varepsilon_\nu \frac{dL_{\varepsilon_{\nu_\mu}}}{d\varepsilon_\nu} &\approx \frac{2}{9}\frac{1}{2000}\varepsilon_n \frac{dL_{\varepsilon_n}}{d\varepsilon_n} \\ &\approx \frac{2}{9}\frac{1}{2000}\frac{1}{2}\min[1, f_{\rm dis}]\varepsilon_A \frac{dL_{\varepsilon_A}}{d\varepsilon_A}, \end{aligned} \tag{23}$$

where $\varepsilon_n(dL_{\varepsilon_n}/d\varepsilon_n)$ is the differential neutron luminosity. Here we have considered that for the tribimaximal mixing of neutrinos from beta decay the flavor ratio on Earth becomes $\nu_e{:}\nu_\mu{:}\nu_\tau \approx 5{:}2{:}2$. This implies that, no matter what the effective optical depth is, the cosmic-ray power is larger than the muon neutrino luminosity by a factor of $\sim 10^4$ and we have

$$L_{\rm CR} \gtrsim 10^4 L_\nu \sim 10^{46}\ {\rm erg\ s^{-1}} \gg L_{\rm bol}, \tag{24}$$

which agrees with our numerical simulations shown in Figure 7. We also note that this conclusion about energetics constraints is insensitive to magnetic fields.

6. Discussions

6.1. Implications for Coronal Environments

We have found that larger values of ξ_B more easily satisfy the Fermi-LAT gamma-ray constraints because of synchrotron cascades (Murase 2022). If the neutrino emission region coincides with the X-ray emission region, i.e., the hot corona, the ion plasma β is

$$\beta = \frac{8\pi n_p k_{\rm B} T_p}{B^2} \approx \frac{\tau_T G M_{\rm BH} m_p}{\sqrt{3}\,\zeta_e \sigma_{\rm T} R^2 U_\gamma}\xi_B^{-1} \approx \left(\frac{\tau_T}{\sqrt{3}\,\zeta_e \lambda_{\rm Edd}}\right)\xi_B^{-1} \tag{25}$$

where $T_p \approx G M_{\rm BH} m_p/(3 k_{\rm B} R)$ is the virial temperature, $n_p \approx \tau_T/(\zeta_e \sigma_T H)$ is the nucleon density of the coronal plasma, H is the coronal scale height, ζ_e is the possible pair multiplication factor, and

$$\frac{\tau_T G M_{\rm BH} m_p}{\sqrt{3}\,\zeta_e \sigma_{\rm T} R^2 U_\gamma} \approx \frac{4\pi \tau_T G M_{\rm BH} m_p c}{\sqrt{3}\,\zeta_e \sigma_{\rm T} L_{\rm bol}} = \frac{\tau_T}{\sqrt{3}\,\zeta_e \lambda_{\rm Edd}}, \tag{26}$$

which is $\sim 0.1-1$ for ion–electron plasma because of $\tau_T \sim 0.1-1$ for X-ray coronae, and $\sqrt{3}\,\lambda_{\rm Edd} \sim 1$ for NGC 1068. Thus, high-β plasma with $\beta \gtrsim 10$ means $\xi_B \lesssim 0.01$–0.1, in which inverse Compton cascades are expected, in which $R \lesssim 3 R_{\rm S}$ should be satisfied. The synchrotron dominance for electromagnetic cascades occurs for $\xi_B \gtrsim 0.1$ (Murase et al. 2020), implying that $\beta \lesssim 1-10$ is necessary to allow $R \sim 10 R_{\rm S}$.

This favors the presence of low-β plasma if hot coronae are responsible for high-energy neutrino emission.[5] Together with our gamma-ray constraints on the emission radius, the most promising particle acceleration mechanisms would be magnetic dissipation, including magnetic reconnections (Kheirandish et al. 2021; Mbarek et al. 2024; Fiorillo et al. 2024) and associated stochastic acceleration in turbulence (Murase et al. 2020; Kimura et al. 2021; Eichmann et al. 2022) although some shock acceleration could be associated with magnetic reconnections (Murase 2022).

If the corona is not magnetically powered with high β, the emission radius has to be even more compact. Although we do not exclude the entire parameter space, at least we exclude shock models with $R \sim 10 R_{\rm S}$–$30 R_{\rm S}$ and weak magnetic fields, which are motivated by Atacama Large Millimeter/submillimeter Array (ALMA) data at the submillimeter band (Inoue et al. 2020). Note that our constraints are even more severe if the contribution of primary nonthermal electrons is included. On the other hand, we also note that this conclusion does not apply if the neutrino emission region is different from the hot corona responsible for X-rays. For example, failed outflows (Alvarez-Muniz & Mészáros 2004; Inoue et al. 2023) and the base of weak jets (Pe'er et al. 2009; Murase 2022) may be viable.

NGC 1068 is known to have a low-power jet with a luminosity of $L_j \sim 10^{43}$ erg s^{-1}, as indicated by radio observations of e-Merlin and the Very Large Array (Mutie et al. 2024), as well as ALMA (Michiyama et al. 2022), through the empirical relationship (Cavagnolo et al. 2010). Knots within these jets may be responsible for gamma-ray emission in the range of $\sim 0.1-1$ GeV (Salvatore et al. 2024). The jet efficiency of jet-quiet AGNs is small, which is $L_j/L_{\rm bol} \sim 0.01-0.1 \ll \lambda_{\rm Edd}$. It is believed that the efficiency of the jet launched via the Blandford–Znajek (BZ) mechanism (Blandford & Znajek 1977) for magnetically arrested disks is high. Based on this, Inoue et al. (2024) speculated that coronae of Seyferts such as NGC 1068 have

---

[5] In the magnetically powered corona model proposed by Murase et al. 2020, the magnetic field B is also considered to be largely turbulent, and the magnetic dissipation power is larger than both the cosmic-ray and intrinsic X-ray luminosities by construction.

$\beta \gtrsim 10-100$. However, such high-β coronae are strongly constrained by multimessenger observations, as shown in this work. Moreover, observationally, a relatively low jet efficiency of $\sim$0.01−0.1 has been inferred even for objects with powerful jets that are presumably launched by the BZ mechanism. The examples include Fanaroff–Riley II jets (Fan & Wu 2019), Fanaroff–Riley 0 jets (Khatiya et al. 2023), and gamma-ray burst jets (e.g., Suwa & Ioka 2011), which could be caused by the time dependence of the magnetic flux and configurations. Low-β coronae without powerful jets have also been inferred from numerical simulations (e.g., Jiang et al. 2019), and the accretion disk may also be strongly magnetized (Hopkins et al. 2024a, 2024b). Recent particle-in-cell (e.g., Grošelj et al. 2024) and magnetohydrodynamic simulations (e.g., Bambic et al. 2023) have also supported that magnetic dissipation in magnetically powered coronae is the most promising mechanism for electron heating.

6.2. Particle Acceleration

Our results support low-β plasma in the coronal region or at the base of possible jets as an acceleration site and disfavor accretion shocks at least for $R \gtrsim 10R_{\rm S}$. Among various possible acceleration processes, magnetic reconnections (e.g., Hoshino 2013, 2015; Guo et al. 2016; Werner et al. 2017; Ball et al. 2018) and stochastic acceleration (e.g., Lynn et al. 2014; Kimura et al. 2016, 2019; Comisso & Sironi 2018; Zhdankin et al. 2019; Lemoine & Malkov 2020; Wong et al. 2020; Lemoine et al. 2024) are promising.

The coronal plasma can be collisionless for ions, although it may not be for electrons, in which stochastic acceleration may operate in the presence of magnetic turbulence. Whether plasma is low β or high β, the timescale is given by

$$\begin{aligned} t_{\rm acc} &\approx \eta_{\rm tur}\left(\frac{c}{V_{\rm A}}\right)^2\frac{H}{c}\left(\frac{\varepsilon_p}{eBH}\right)^{2-q} \\ &\simeq 1.8\times10^4\ {\rm s}\ \eta_{\rm tur,1}\beta_{-1}\left(\frac{R}{10R_{\rm S}}\right)^2\left(\frac{M_{\rm BH}}{10^7\ M_\odot}\right) \\ &\times\left(\frac{\varepsilon_p}{eBH}\right)^{2-q}, \end{aligned} \tag{27}$$

where $\eta_{\rm tur}$ is a parameter representing the efficiency of stochastic acceleration, $q \sim 1.5-2$ describes the energy dependence of the diffusion coefficient, and $V_{\rm A} = B/\sqrt{4\pi m_p n_p}$ is the Alfvén velocity.

For cosmic-ray protons with energy around 100−1000 TeV, the dominant cooling timescale is the Bethe–Heitler pair production cooling, which is

$$\begin{aligned} t_{\rm BH} &\approx \frac{1}{\tilde{n}_{\rm disk}\hat{\sigma}_{\rm BH}c} \\ &\simeq 1.4\times10^3\ {\rm s}\ \tilde{L}_{\rm disk,\,44.7}^{-1}\left(\frac{R}{10R_{\rm S}}\right)^2\left(\frac{M_{\rm BH}}{10^7\ M_\odot}\right)^2 \\ &\times\left(\frac{\varepsilon_{\rm disk}}{31.5\ {\rm eV}}\right), \end{aligned} \tag{28}$$

and the balance between acceleration and cooling timescales, $t_{\rm acc} \sim t_{\rm BH}$, may give $\varepsilon_p^{\rm max} \sim \mathcal{O}(100)$ TeV.

Particles may also be accelerated by magnetic reconnections. The magnetization parameter is

$$\begin{aligned} \sigma &= \frac{B^2}{4\pi n_p m_p c^2} = \beta^{-1}\left(\frac{2k_{\rm B}T_p}{m_p c^2}\right) = \beta^{-1}\left(\frac{R_{\rm S}}{3R}\right) \\ &= \frac{2\xi_B\zeta_e L_{\rm bol}\sigma_{\rm T}}{\sqrt{3}\,\tau_T m_p c^2 R} \\ &\simeq 4.7\times10^{-2}\frac{\xi_B\zeta_e}{\tau_T}L_{\rm bol,\,45}\left(\frac{R}{10R_{\rm S}}\right)^{-1}\left(\frac{M_{\rm BH}}{10^7\ M_\odot}\right)^{-1}. \end{aligned} \tag{29}$$

Particle acceleration via magnetic reconnections is efficient and leads to hard spectra for $\sigma > 1$. For $R \lesssim 30R_{\rm S}$, this requires $\beta \lesssim 0.01-1$, so very low β plasma environments are necessary, and extreme magnetization parameters such as $\sigma \gtrsim 10^4$ have been considered (Mbarek et al. 2024; Fiorillo et al. 2024). The acceleration timescale is

$$\begin{aligned} t_{\rm acc} &\approx \eta\frac{\varepsilon_p}{eBc} \\ &\simeq (0.013\ {\rm s})\eta_1\left(\frac{R}{10R_{\rm S}}\right)\xi_B^{-1/2}L_{\rm bol,\,45}^{-1/2}\left(\frac{M_{\rm BH}}{10^7\ M_\odot}\right) \\ &\times\left(\frac{\varepsilon_p}{100\ {\rm TeV}}\right), \end{aligned} \tag{30}$$

where η is a coefficient describing the efficiency of acceleration via magnetic reconnections. At higher energies, the dominant cooling process becomes the photomeson production, whose timescale is given by

$$\begin{aligned} t_{p\gamma} &\approx \frac{1}{\tilde{n}_{\rm disk}\hat{\sigma}_{p\gamma}c} \\ &\simeq 16\ \ {\rm s}\ \tilde{L}_{\rm disk,\,44.7}^{-1}\left(\frac{R}{10R_{\rm S}}\right)^2\left(\frac{M_{\rm BH}}{10^7\ M_\odot}\right)^2 \\ &\times\left(\frac{\varepsilon_{\rm disk}}{31.5\ {\rm eV}}\right), \end{aligned} \tag{31}$$

for cosmic-ray protons at sufficiently high energies. The condition $t_{\rm acc} \sim t_{p\gamma}$ gives a maximum energy of $\varepsilon_p^{\rm max} \sim \mathcal{O}(10)$ PeV.

In the leptonic scenario, the acceleration timescale of electrons is

$$t_{\rm acc} \approx \eta\frac{\varepsilon_e}{eBc}, \tag{32}$$

and the balance between the synchrotron and inverse Compton cooling gives the electron maximum energy,

$$\begin{aligned} \varepsilon_e^{\rm max} &\approx \left(\frac{6\pi e}{\sigma_{\rm T}B\eta(1+Y)}\right)^{1/2}m_e c^2 \\ &\simeq 0.64\ \ {\rm TeV}\ [\eta(1+Y)]^{-1/2}\left(\frac{R}{10R_{\rm S}}\right)^{1/2}\xi_B^{-1/4} \\ & L_{\rm bol,\,45}^{-1/4}, \end{aligned} \tag{33}$$

where Y denotes the inverse Compton Y parameter. The maximum energy required for the leptonic scenario is realized only if the magnetic field is sufficiently weak.

In the strongly magnetized plasma, the inverse Compton emission is highly suppressed. Note that the maximum synchrotron energy is limited as

$$\varepsilon_{\mathrm{syn}\gamma}^{\max} \approx \frac{3heB}{4\pi m_e c}\left(\frac{\varepsilon_e^{\max}}{m_e c^2}\right)^2 \simeq 240\ \mathrm{MeV}[\eta(1+\mathrm{Y})]^{-1}, \quad (34)$$

which is the so-called synchrotron burnoff limit (Guilbert et al. 1983; Aharonian et al. 2002; Zhang 2018), independent of the magnetic field strength. This energy is much below 10 TeV, being insufficient for the leptonic scenario.

6.3. Impacts of Other Parameters

In this work, we adopt $V = 0.1c$ as the default velocity of the system. We note that the velocity can be smaller, which affects effective optical depths through t_{dyn}. For example, the infall velocity is estimated to be

$$V_{\mathrm{fall}} = \alpha V_{\mathrm{K}} \sim 0.01c\alpha_{-1}(R/R_{\mathrm{S}})^{-1/2}, \quad (35)$$

where α is the viscous parameter in the accreting flow and $V_{\mathrm{K}} = \sqrt{GM_{\mathrm{BH}}/R} = c/\sqrt{2(R/R_{\mathrm{S}})}$ is the Keplerian velocity. The effective optical depth to photomeson production is larger with smaller velocities, in which the cosmic-ray luminosity requirement can be relaxed, especially for large values of R. For the photohadronic scenario, in the limit that the system is calorimetric, the cosmic-ray luminosity is required to be $L_{\mathrm{CR}} \gtrsim 10^{43} f_{\mathrm{sup}}^{-1}$ erg s^{-1}, which is consistent with the conclusion by Murase (2022), although our constraint is tighter, due to the suppression factor by the Bethe–Heitler process. Similarly, for the beta-decay scenario, the efficiency is higher, so that the power requirement is relaxed for large radii, but it cannot be below $\sim 10^{46}$ erg s^{-1}. On the other hand, the gamma-ray power requirement in the leptonic scenario is not affected because $\tau_{\gamma\gamma\rightarrow e^+e^-} \gg 1$ is satisfied.

Although we primarily focus on $p\gamma$ scenarios, one may consider pp scenarios, where neutrinos are mostly produced via inelastic collisions between cosmic rays and plasma gas (Inoue et al. 2020; Murase et al. 2020; Eichmann et al. 2022). The effective optical depth for inelastic pp cooling rate is estimated to be

$$\begin{aligned} f_{pp} &\approx n_p \hat{\sigma}_{pp} R(c/V) \\ &\simeq 0.26\ (\tau_T/0.5)\left(\frac{V}{0.1c}\right)^{-1}, \end{aligned} \quad (36)$$

where $\hat{\sigma}_{pp} \sim 2 \times 10^{-26}$ cm^2 is the effective pp cross section including the inelasticity, $n_p \approx \tau_T/(\zeta_e \sigma_{\mathrm{T}} H)$ is the nucleon density in the corona region, and $\tau_T \sim 0.1-1$. Based on the comparison with Equation (6), we see that the pp process can be more important than the $p\gamma$ process at large emission radii. However, our conclusions for $\xi_B \lesssim 0.1$ would remain the same because cascades from photohadronic processes are more relevant at small emission radii, while $R = 30R_{\mathrm{S}}$ is allowed for $\xi_B \sim 1$ (Murase 2022; Ajello et al. 2023).

Finally, we comment on the flavor ratio. In the standard hadronic scenarios, the approximate flavor ratio observed on Earth is expected to be ν_e:ν_μ:$\nu_\tau \approx$ 1:1:1, which is assumed in the IceCube data shown in Figure 2. However, the flavor ratio varies among different mechanisms, and we have

$$\begin{aligned} &\nu_e\colon \nu_\mu\colon \nu_\tau \approx 1\colon 1\colon 1 \quad \text{(hadronic)} \\ &\nu_e\colon \nu_\mu\colon \nu_\tau \approx 14\colon 11\colon 11 \quad \text{(leptonic)} \\ &\nu_e\colon \nu_\mu\colon \nu_\tau \approx 5\colon 2\colon 2 \quad \text{(beta decay).} \end{aligned} \quad (37)$$

Correspondingly, in Figures 4 and 6, different flavor ratios are assumed when the IceCube data are depicted. The determination of neutrino flavors with future observations will also be relevant as an independent method to discriminate among different neutrino production mechanisms (e.g., Beacom et al. 2003; Shoemaker & Murase 2016; Bustamante & Ahlers 2019). The IceCube Collaboration has analyzed the flavor composition using all-sky neutrino data (Aartsen et al. 2015a, 2015b; Lad & Cowen 2023). It has been proposed that AGNs like NGC 1068 can account for the all-sky neutrino flux in the 10−100 TeV range (Murase et al. 2020), and the all-sky neutrino data can also be used to discriminate among different production mechanisms. In particular, the beta-decay scenario has already been ruled out as the dominant neutrino production mechanism (Bustamante & Ahlers 2019).

7. Summary

In this study, based on the recent multimessenger observations including IceCube and Fermi-LAT data, we constrained the cosmic-ray luminosity and emission radius that are compatible with Seyfert II galaxy NGC 1068. Our results are summarized as follows.

1. In the photohadronic scenario, the emission radius is constrained to $R \lesssim 3R_{\mathrm{S}}-15R_{\mathrm{S}}$. These results support the previous findings by Murase (2022), but thanks to the updated Fermi-LAT data (Ajello et al. 2023), our constraints are stronger. For these emission radii, the required minimum cosmic-ray proton luminosity in the energy range of 10−30 TeV is $L_{\mathrm{CR}} \gtrsim (3-10) \times 10^{43}$ erg s^{-1} (see also Section 2.3 of Murase 2022). The minimum cosmic-ray luminosity can be lower than the total X-ray luminosity, which is also consistent with considerations from the all-sky neutrino and gamma-ray flux data (Murase et al. 2016).
2. In the leptonic scenario, neutrinos come from the muon–antimuon pair production (Hooper & Plant 2023). We found that cascaded gamma rays always overshoot gamma-ray and/or X-ray data. The muon pair production efficiency is too low when coronal X-ray emission is considered as a target photon field. This conclusion remains unchanged when the effects of nonlinear electromagnetic cascades are taken into account, which makes our conclusion more robust. We showed that the minimum gamma-ray luminosity is $L_\gamma \sim 10^{47}$ erg s^{-1} both analytically and numerically, which largely exceeds the Eddington luminosity. We further argued that it is challenging to accelerate electrons up to 10 TeV energies in strongly magnetized plasma. From the above three general arguments, we conclude that the leptonic scenario is unlikely as a viable mechanism for neutrino emission from NGC 1068.
3. In the beta-decay scenario, neutrinos mainly originate from neutrons generated via the photodisintegration of nuclei (Yasuda et al. 2024). With AMES, which

quantitatively handles details on the spectrum of neutrons from the disintegration and subsequent beta-decay spectra, we found that inverse Compton emission by beta-decay electrons violates the gamma-ray data when observed infrared photons from the dust torus are considered. This conclusion is robust when the inevitable contribution from the Bethe–Heitler pair production is considered, and even stronger when the photomeson production is consistently included. We also showed that the minimum cosmic-ray power to explain the neutrino data in this scenario, $L_{\rm CR} \gtrsim 10^{46}$ erg s^{-1}, largely exceeds the Eddington luminosity, by which we concluded that the beta-decay scenario is excluded.

4. Our results support the standard neutrino production mechanisms that high-energy neutrinos are produced by pp or $p\gamma$ processes, which require compact emission radii (Murase 2022), and rule out the leptonic and neutron-decay scenarios without depending on any details of the models. Our conclusions rely on two different general arguments: X-ray/gamma-ray constraints and cosmic-ray energetics required by neutrino observations. In particular, the former is robust because the ratio of electromagnetic to neutrino components is relevant without depending on the values of optical depths such as $\tau_{\gamma\gamma\to\mu^+\mu^-}$ and $f_{\rm dis}$ themselves. In the photohadronic scenario, we found that the gamma-ray constraints on R depend on ξ_B, depending on whether cascades primarily occur via synchrotron or inverse Compton processes. For $\xi_B \lesssim 0.1$ corresponding to $\beta \gtrsim 10$, electromagnetic cascades occur via inverse Compton emission, in which the Fermi-LAT data led to $R \lesssim 3R_{\rm S}$. This disfavors high-β plasma regions as particle acceleration sites, and accretion shock models with $R \gtrsim 10R_{\rm S}$–$30R_{\rm S}$ (e.g., Inoue et al. 2020) are unlikely. On the other hand, for $\xi_B \gtrsim 1$ corresponding to $\beta \lesssim 0.1$, the gamma-ray constraint on the emission region is relaxed to $R \lesssim 15R_{\rm S}$, which is consistent with the magnetically powered corona model (Murase et al. 2020).

We showed that the main production mechanism for high-energy neutrinos from NGC 1068 must be either the photohadronic ($p\gamma$) or hadronuclear (pp) mechanism. Our results demonstrated how multimessenger modeling of neutrino and gamma-ray data can be used for revealing and constraining neutrino production mechanisms. We also obtained some implications for possible acceleration mechanisms through cosmic-ray energetics constraints and constraints on neutrino emission regions. The calculations presented in this work are applicable to not only NGC 1068 but also other AGNs such as NGC 4151 and NGC 4945 (Murase et al. 2024). As discussed in this work, measurements of the neutrino flavor ratios are also useful as a complementary way of confirming our conclusion.

Acknowledgments

First of all, we thank the reviewer for his valuable comments. We thank Mukul Bhattacharya, Carlos Blanco, and Mainak Mukhopadhyay for the useful discussions. The research by A. D. and K.M. is supported by the NSF grant No. AST-2308021. The work of K.M. is supported by NSF grant Nos. AST-2108466 and AST-2108467. The research by B.T.Z. and K.M. is supported by KAKENHI grant No. 20H05852.

ORCID iDs

Abhishek Das https://orcid.org/0000-0003-2916-0211
B. Theodore Zhang https://orcid.org/0000-0003-2478-333X
Kohta Murase https://orcid.org/0000-0002-5358-5642

References

Aartsen, M. G., Abbasi, R., Abdou, Y., et al. 2013a, PhRvL, 111, 021103
Aartsen, M. G., Abbasi, R., Abdou, Y., et al. 2013b, Sci, 342, 1242856
Aartsen, M. G., Ackermann, M., Adams, J., et al. 2015a, PhRvL, 114, 171102
Aartsen, M. G., Abraham, K., Ackermann, M., et al. 2015b, ApJ, 809, 98
Abbasi, R., Ackermann, M., Adams, J., et al. 2022, Sci, 378, 538
Abdollahi, S., Acero, F., Ackermann, M., et al. 2020, ApJS, 247, 33
Acciari, V. A., Ansoldi, S., Antonelli, L. A., et al. 2019, ApJ, 883, 135
Aharonian, F., & Taylor, A. M. 2010, APh, 34, 258
Aharonian, F. A., Belyanin, A. A., Derishev, E. V., Kocharovsky, V. V., & Kocharovsky, V. V. 2002, PhRvD, 66, 023005
Ajello, M., Murase, K., & McDaniel, A. 2023, ApJL, 954, L49
Ajello, M., Angioni, R., Axelsson, M., et al. 2020, ApJ, 892, 105
Alvarez-Muniz, J., & Mészáros, P. 2004, PhRvD, 70, 123001
Athar, H., Lin, G.-L., & Tseng, J.-J. 2001, PhRvD, 64, 071302
Ball, D., Sironi, L., & Özel, F. 2018, ApJ, 862, 80
Bambic, C. J., Quataert, E., & Kunz, M. W. 2023, MNRAS, 527, 2895
Bauer, F. E., Arévalo, P., Walton, D. J., et al. 2015, ApJ, 812, 116
Beacom, J. F., Bell, N. F., Hooper, D., Pakvasa, S., & Weiler, T. J. 2003, PhRvD, 68, 093005
Bhattacharjee, P., & Sigl, G. 2000, PhR, 327, 109
Blandford, R. D., & Znajek, R. L. 1977, MNRAS, 179, 433
Bustamante, M., & Ahlers, M. 2019, PhRvL, 122, 241101
Capanema, A., Esmaili, A., & Murase, K. 2020, PhRvD, 101, 103012
Cavagnolo, K. W., McNamara, B. R., Nulsen, P. E. J., et al. 2010, ApJ, 720, 1066
Chodorowski, M. J., Zdziarski, A. A., & Sikora, M. 1992, ApJ, 400, 181
Comisso, L., & Sironi, L. 2018, PhRvL, 121, 255101
Courtois, H. M., Pomarede, D., Tully, R. B., & Courtois, D. 2013, AJ, 146, 69
Eichmann, B., Oikonomou, F., Salvatore, S., Dettmar, R.-J., & Becker Tjus, J. 2022, ApJ, 939, 43
Fan, X.-L., & Wu, Q. 2019, ApJ, 879, 107
Fang, K., Gallagher, J. S., & Halzen, F. 2022, ApJ, 933, 190
Fang, K., & Murase, K. 2018, NatPh, 14, 396
Fiorillo, D. F. G., Petropoulou, M., Comisso, L., Peretti, E., & Sironi, L. 2024, ApJL, 961, L14
García-Burillo, S., Combes, F., Ramos Almeida, C., et al. 2019, A&A, 632, A61
Gilmore, R. C., Somerville, R. S., Primack, J. R., & Dominguez, A. 2012, MNRAS, 422, 3189
Grošelj, D., Hakobyan, H., Beloborodov, A. M., Sironi, L., & Philippov, A. 2024, PhRvL, 132, 085202
Guilbert, P. W., Fabian, A. C., & Rees, M. J. 1983, MNRAS, 205, 593
Guo, F., Li, X., Li, H., et al. 2016, ApJL, 818, L9
Hooper, D., & Plant, K. 2023, PhRvL, 131, 231001
Hopkins, P. F., Squire, J., Quataert, E., et al. 2024a, OJAp, 7, 20
Hopkins, P. F., Squire, J., Su, K.-Y., et al. 2024b, OJAp, 7, 19
Hoshino, M. 2013, ApJ, 773, 118
Hoshino, M. 2015, PhRvL, 114, 061101
Imanishi, M., Nakanishi, K., & Izumi, T. 2016, ApJL, 822, L10
Inoue, S., Cerruti, M., Murase, K., & Liu, R. Y. 2023, PoS, 444, 1161
Inoue, Y., Khangulyan, D., & Doi, A. 2020, ApJL, 891, L33
Inoue, Y., Takasao, S., & Khangulyan, D. 2024, arXiv:2401.07580
Jiang, Y.-F., Blaes, O., Stone, J. M., & Davis, S. W. 2019, ApJ, 885, 144
Karakula, S., Kociolek, G., Moskalenko, I. V., & Tkaczyk, W. 1994, ApJS, 92, 481
Khatiya, N. S., Boughelilba, M., Karwin, C. M., et al. 2023, arXiv:2310.19888
Kheirandish, A., Murase, K., & Kimura, S. S. 2021, ApJ, 922, 45
Kimura, S. S., Murase, K., & Mészáros, P. 2021, NatCo, 12, 5615
Kimura, S. S., Murase, K., & Toma, K. 2015, ApJ, 806, 159
Kimura, S. S., Toma, K., Suzuki, T. K., & Inutsuka, S. I. 2016, ApJ, 822, 88
Kimura, S. S., Tomida, K., & Murase, K. 2019, MNRAS, 485, 163
Lad, N., & Cowen, D. F. 2023, arXiv:2308.15213
Lemoine, M., & Malkov, M. A. 2020, MNRAS, 499, 4972
Lemoine, M., Murase, K., & Rieger, F. 2024, PhRvD, 109, 063006
Li, Z., & Waxman, E. 2007, arXiv:0711.4969
Lynn, J. W., Quataert, E., Chandran, B. D. G., & Parrish, I. J. 2014, ApJ, 791, 71

Marinucci, A., Bianchi, S., Matt, G., et al. 2016, MNRAS, 456, L94

Mbarek, R., Philippov, A., Chernoglazov, A., Levinson, A., & Mushotzky, R. 2024, PhRvD, 109, L101306, arXiv:2310.15222

Michiyama, T., Inoue, Y., Doi, A., & Khangulyan, D. 2022, ApJL, 936, L1

Murase, K. 2018, PhRvD, 97, 081301

Murase, K. 2022, ApJL, 941, L17

Murase, K., Ahlers, M., & Lacki, B. C. 2013, PhRvD, 88, 121301

Murase, K., & Beacom, J. F. 2010a, PhRvD, 81, 123001

Murase, K., & Beacom, J. F. 2010b, PhRvD, 82, 043008

Murase, K., Guetta, D., & Ahlers, M. 2016, PhRvL, 116, 071101

Murase, K., Karwin, C. M., Kimura, S. S., Ajello, M., & Buson, S. 2024, ApJL, 961, L34

Murase, K., Kimura, S. S., & Meszaros, P. 2020, PhRvL, 125, 011101

Murase, K., & Stecker, F. W. 2023, The Encyclopedia of Cosmology (Singapore: World Scientific)

Murase, K., & Waxman, E. 2016, PhRvD, 94, 103006

Mutie, I. M., Williams-Baldwin, D., Beswick, R. J., et al. 2024, MNRAS, 527, 11756

Padovani, P., Gilli, R., Resconi, E., Bellenghi, C., & Henningsen, F. 2024, A&A, 684, L21

Panessa, F., Bassani, L., Cappi, M., et al. 2006, A&A, 455, 173

Pe’er, A., Murase, K., & Mészáros, P. 2009, PhRvD, 80, 123018

Rosas, V. G., Isbell, J. W., Jaffe, W., et al. 2022, Natur, 602, 403

Salvatore, S., Eichmann, B., Rodrigues, X., Dettmar, R. J., & Becker Tjus, J. 2024, A&A, 687, A139

Shakura, N. I., & Sunyaev, R. A. 1973, A&A, 24, 337

Shoemaker, I. M., & Murase, K. 2016, PhRvD, 93, 085004

Suwa, Y., & Ioka, K. 2011, ApJ, 726, 107

Svensson, R. 1987, MNRAS, 227, 403

Tikhonov, N. A., & Galazutdinova, O. A. 2021, AstBu, 76, 255

Tully, R. B., Rizzi, L., Shaya, E. J., et al. 2009, AJ, 138, 323

Werner, G. R., Uzdensky, D. A., Begelman, M. C., Cerutti, B., & Nalewajko, K. 2017, MNRAS, 473, 4840

Wong, K., Zhdankin, V., Uzdensky, D. A., Werner, G. R., & Begelman, M. C. 2020, ApJL, 893, L7

Woo, J.-H., & Urry, C. M. 2002, ApJ, 579, 530

Workman, R. L., Burkert, V. D., Crede, V., et al. 2022, PTEP, 2022, 083C01

Yasuda, K., Inoue, Y., & Kusenko, A. 2024, arXiv:2405.05247

Zhang, B. 2018, The Physics of Gamma-Ray Bursts (Cambridge: Cambridge Univ. Press)

Zhang, B.-B., Zhang, B., Murase, K., Connaughton, V., & Briggs, M. S. 2014, ApL, 787, 66

Zhang, B. T., & Murase, K. 2023, MNRAS, 524, 76

Zhdankin, V., Uzdensky, D. A., Werner, G. R., & Begelman, M. C. 2019, PhRvL, 122, 055101